Received: 30 March 2024 | Revised: 3 July 2024 | Accepted: 1 September 2024

DOI: 10.1002/fld.5335

RESEARCH ARTICLE

WILEY

# Novel lattice Boltzmann method for simulation of strongly shear thinning viscoelastic fluids

**Richard Kellnberger**[1] | **Tomasz Jüngst**[2] | **Stephan Gekle**[1]

[1]Biofluid Simulation and Modeling - Theoretische Physik VI, Universität Bayreuth, Bayreuth, Germany

[2]Department of Functional Materials in Medicine and Dentistry Institute of Functional Materials and Biofabrication (IFB) and KeyLab Polymers for Medicine of the Bavarian Polymer Institute (BPI), Universität Würzburg, Würzburg, Germany

**Correspondence**
Richard Kellnberger, Biofluid Simulation and Modeling - Theoretische Physik VI, Universität Bayreuth, Bayreuth, Germany.
Email:
Richard.Kellnberger@uni-bayreuth.de

**Funding information**
Deutsche Forschungsgemeinschaft, Grant/Award Number: 326998133; Federal Ministry of Education and Research, Grant/Award Number: 13XP5071B

**Abstract**

The simulation of viscoelastic liquids using the Lattice–Boltzmann method (LBM) in full three dimensions remains a formidable numerical challenge. In particular the simulation of strongly shear-thinning fluids, where the ratio between the high-shear and low-shear viscosities is large, is often prevented by stability problems. Here we present a novel approach to overcome this issue. The central idea is to artificially increase the solvent viscosity which allows the method to benefit from the very good stability properties of the LBM. To compensate for this additional viscous stress, the polymer stress is reduced by the same amount. We apply this novel method to simulate two realistic cell carrier fluids, methyl cellulose and alginate solutions, of which the latter exhibits a viscosity ratio exceeding 10,000.

**KEYWORDS**

biofluidics, immersed boundary, laminar flow, lattice Boltzmann, microfluidics, non-Newtonian, stability

## 1 | INTRODUCTION

Microfluidic technologies involving living cells are becoming increasingly popular. Examples include medical diagnostics, where the pathological alteration of cell properties can serve as a marker for disease detection[1] or biofabrication where living cells are printed to create artificial tissues.[2–4] In all these applications cells are suspended in a cell carrier fluid which typically contains dissolved polymers making the fluid highly viscoelastic and shear-thinning. The motivation behind using viscoelastic fluids differs between applications. In medical diagnostics, the viscous stress must be large enough to achieve detectable cell deformation, while in biofabrication the printed construct must be stable enough to retain its shape after the printing process. To satisfy the latter requirement, cell carriers used in biofabrication ("bioinks") typically exhibit a very high viscosity ratio with the zero-shear viscosity being many orders of magnitude larger than the pure solvent viscosity.[5]

To understand the rheology of such complex liquids in non-trivial geometries, computer simulations are an invaluable tool. While a number of numerical techniques have been developed, the simulation of viscoelastic liquids remains an involved subject,[6] in particular for high viscosity ratios. A very popular simulation technique for Newtonian fluids is the Lattice–Boltzmann method (LBM)[7] due to its simplicity and high parallelizability. LBM has also been extended to viscoelastic situations, mainly in two[8–24] but occasionally also in three[25–36] dimensions. We will discuss these approaches in detail in Section 3 below. To alleviate stability problems, some of these works include an artificial diffusivity of the polymer stress,[25,29,31,34] or perform special decompositions of the stress tensor.[13] Despite these improvements, however, none of these methods has been applied to very high viscosity ratio fluids which are often used as cell carrier fluids in lab experiments or technological applications.

To fill this gap, here we develop a new variant of viscoelastic LBM which allows the stable and accurate simulation of very high viscosity ratio fluids. Our technique is based on the insight that stability issues in traditional viscoelastic LBMs arise due to an imbalance between the very large polymer stress and the much smaller viscous stress of the solvent. We overcome this issue by moving ("shuffling") part of the polymer stress into the viscous part of the LBM algorithm.

## 2 | RHEOLOGY OF CELL CARRIER FLUIDS

### 2.1 | Experimental data

To illustrate our novel LBM algorithm, we consider two prototypical cell carrier fluids. The first is an alginate solution which is often used in biofabrication but can also serve as a common food additive. Our solution contains 4 % w/v alginate dissolved in ultrapure water and was measured in a commercial plate-plate rheometer (see Appendix A for experimental details). The shear-dependent viscosity $\eta$ and the first normal stress difference $N_1$ are shown as function of shear rate in Figure 1. We note the very high zero-shear viscosity of more than 10,000 mPa s. Bioinks in biofabrication are in general characterized by such high viscosities to guarantee stability of the printed construct. At the same time, during the actual printing process when the material is flowing, the viscosity should be as low as possible to avoid excessive mechanical stress on the embedded cells. This motivates the use of highly shear-thinning viscoelastic fluids in biofabrication.

The second cell carrier fluid modeled in this work is a methyl cellulose solution which is commonly used in real-time-deformation-cytometry (RT-DC) experiments. RT-DC experiments allow very high-throughput measurements of cell mechanical properties and have been used successfully for disease detection by screening blood samples. We extract our data from Reference 37 where the shear rheology of methyl cellulose was measured using a plate-plate and cone-plate rheometer. Three concentrations of 0.49%, 0.59% and 0.83% methyl cellulose in phosphate buffered saline (PBS) were investigated, and their rheology is shown in Figure 2.

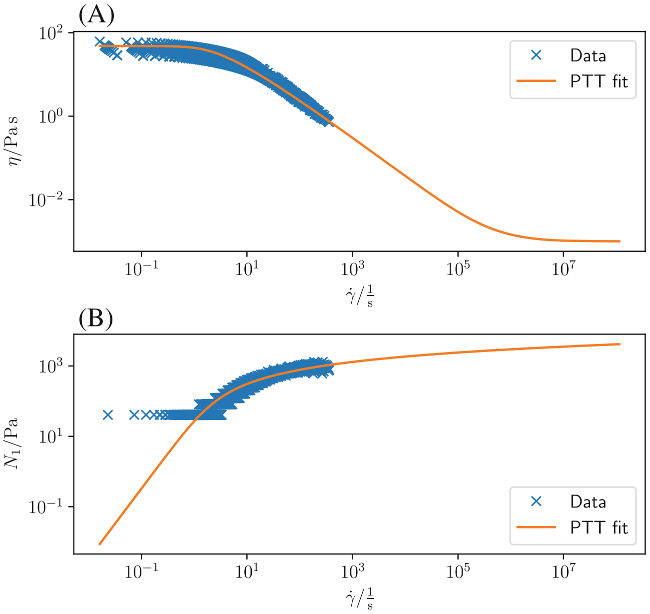

**FIGURE 1** Rheology data for alginate solution from 21 measurements of the viscosity (A) and normal stress (B). Orange lines show a fit of the Phan-Thien and Tanner (PTT) rheological model. [Colour figure can be viewed at wileyonlinelibrary.com]

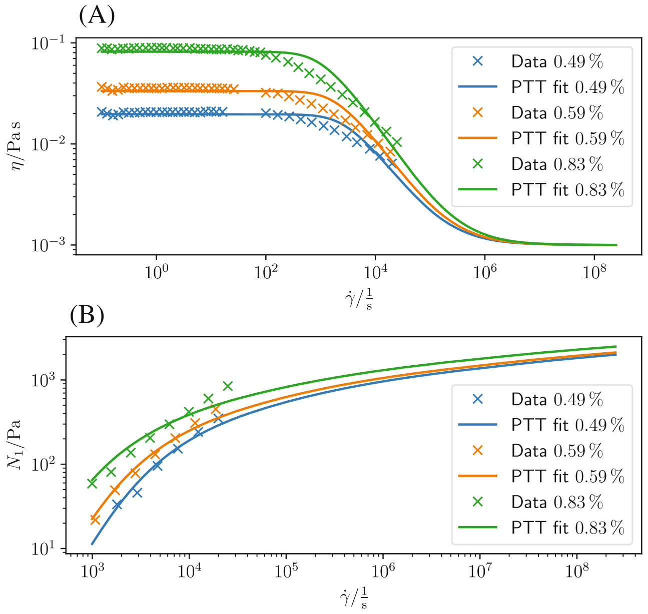

**FIGURE 2** The viscosity (A) and normal stress (B) of a methyl cellulose solution from Reference 37. Lines show a fit of the Phan-Thien and Tanner (PTT) rheological model.

## 2.2 | Fitting data with the PTT model

Due to the complexity of viscoelastic fluids, there is an abundance of (semi-)empirical models to describe rheological data. Common options include the Oldroyd-B[38] and the FENE-P model.[39,40] The Oldroyd-B model is not appropriate for most real complex fluids as it features a shear-independent viscosity in clear contradiction to the experimental data presented in Figures 1 and 2. A good fit to our data was obtained with the so-called Phan-Thien and Tanner (PTT) model by Phan-Thien and Tanner[41] and Phan-Thien[42] which has been developed explicitly for polymer networks in solution and thus appears to capture well the essential physics behind the alginate and methyl cellulose solutions.

The PTT model can be written in the form of a differential equation for the polymer stress $\underline{\tau}$[43]:

$$\overset{\nabla}{\underline{\tau}} = -\xi(\underline{\tau}\cdot\underline{D}+\underline{D}\cdot\underline{\tau}) - e^{\frac{\epsilon\lambda}{\eta_\mathrm{p}}\mathrm{Tr}\underline{\tau}}\frac{\underline{\tau}}{\lambda} + 2\frac{\eta_\mathrm{p}}{\lambda}\underline{D}, \tag{1}$$

where $\underline{D}$ is the strain rate tensor. We note that Reference 43 have also studied extended forms of the PTT model with a Mittag–Leffler instead of an exponential function, whereas here we restrict ourselves to the exponential version. The polymer viscosity is denoted $\eta_\mathrm{p}$ and $\lambda$ is the corresponding relaxation time. $\epsilon$ is the so-called extensibility parameter which controls at which shear rates thinning takes place and $\xi$ describes the slip in the polymer network which we will set to zero in the following. The upper convected derivative of an arbitrary tensor $\underline{A}$ is defined as follows:

$$\overset{\nabla}{\underline{A}} = \frac{\mathrm{D}\underline{A}}{\mathrm{D}t} - \left((\nabla\vec{u})^\mathrm{T}\cdot\underline{A}+\underline{A}\cdot(\nabla\vec{u})\right), \tag{2}$$

where $\vec{u}$ is the fluid velocity and $(\nabla\vec{u})_{ij} = \nabla_i\vec{u}_j$. The material derivative is

$$\frac{\mathrm{D}\underline{A}}{\mathrm{D}t} = \frac{\partial\underline{A}}{\partial t} + (\vec{u}\cdot\nabla)\underline{A}. \tag{3}$$

Finally, the total fluid stress $\underline{\sigma}$ is the sum of the polymer stress $\underline{\tau}$ and a solvent stress due to the Newtonian solvent with viscosity $\eta_\mathrm{s}$:

$$\underline{\sigma} = \underline{\tau} + 2\eta_\mathrm{s}\underline{D}. \tag{4}$$

**TABLE 1** Parameters of the PTT model obtained by fitting to the rheological measurements in Figures 1 and 2 along with corresponding viscosity ratios from Equation (7).

| Fluid | $\eta_p$/mPa s | $\lambda$/ms | $\epsilon$ | $R_\eta$ |
|---|---|---|---|---|
| alginate 4% w/v | $(48.2 \pm 0.4) \times 10^3$ | $343 \pm 4$ | $0.545 \pm 0.010$ | $4.82 \times 10^4$ |
| methyl c. 0.49% | $18.7 \pm 0.4$ | $0.344 \pm 0.003$ | $0.270 \pm 0.003$ | 18.7 |
| methyl c. 0.59% | $32.5 \pm 0.7$ | $0.433 \pm 0.004$ | $0.365 \pm 0.004$ | 32.5 |
| methyl c. 0.83% | $81 \pm 2$ | $0.714 \pm 0.009$ | $0.496 \pm 0.006$ | 81 |

**TABLE 2** Compilation of literature data on typical bioinks showing that a very viscosity ratio $R_\eta$ is a generic feature of these liquids.

| Author | Material | $\eta_0$/Pa s | $\eta_\infty$/Pa s | $R_\eta$ | Extracted from |
|---|---|---|---|---|---|
| Amorim[46] | Pre-crosslinked alginate | $> 1 \times 10^4$ | $< 3 \times 10^{-1}$ | $> 3 \times 10^4$ | Figure 3B |
| Pössl[2] | Blend | $2 \times 10^2$ | $5 \times 10^{-1}$ | $4 \times 10^2$ | Figure 4 |
| Paxton[5] | Alginate | $5 \times 10^4$ | $< 5 \times 10^1$ | $> 1 \times 10^3$ | Figure 4B |
| Jalaal[47] | Pluronic F-127 | $> 1 \times 10^3$ | $< 1 \times 10^{-1}$ | $> 1 \times 10^4$ | Figure 6E |

For a simple shear flow in the $xy$-plane of a PTT fluid with $\xi = 0$, an analytical expression for $\eta$ and $N_1$ can be derived as detailed in Appendix B:

$$\eta(\dot{\gamma}) = \frac{\eta_p}{\exp\left[0.5 W_0\left(4\epsilon \mathrm{Wi}^2\right)\right]} + \eta_s, \tag{5}$$

$$N_1 = \frac{\eta_p}{2\epsilon\lambda} W_0\left(4\epsilon \mathrm{Wi}^2\right), \tag{6}$$

where $\mathrm{Wi} = \lambda\dot{\gamma}$ is the Weissenberg number and $W_0$ is the Lambert $W$-function. Fitting these equations to the rheological data for alginate and methyl cellulose leads to satisfactory agreement as shown in Figures 1 and 2. In the fit, the solvent viscosity was fixed at $\eta_s = 1$ mPa s as the viscosity of the PBS buffer. The obtained parameters are given in Table 1.

We introduce the ratio between the polymer and the solvent viscosity and express it as a ratio between the viscosity at zero shear rate, $\eta_0$, and the viscosity at infinite shear rate $\eta_\infty$:

$$R_\eta = \frac{\eta_p}{\eta_s} = \frac{\eta_0 - \eta_\infty}{\eta_\infty}, \tag{7}$$

which we and others found to be an important parameter to determine numerical stability of LB simulations, especially if no artificial diffusivity is used.[17,25] This ratio can similarly be defined for other models such as FENE-P or the inelastic, but shear-thinning Carreau-Yasuda model[44,45] using the zero-shear viscosity $\eta_0$ and the infinite-shear viscosity $\eta_\infty$. For our alginate solution we obtain $R_\eta = (48.2 \pm 0.4) \times 10^3$, indicating that the solution viscosity at very low shear rates is more than four orders of magnitude larger than the solvent viscosity which represents a severe challenge to standard numerical algorithms. That this characteristic is not unique to alginate, but is in fact a generic feature of cell carrier fluids used in bioprinting is shown in Table 2 where rheological data from various literature sources have been compiled into a single format to determine $R_\eta$. The 0.49% methyl cellulose solution used in RT-DC measurements, in contrast, features a much lower value of $R_\eta = 18.7 \pm 0.4$.

## 3 | EXISTING LBM METHODS

Since the early days of LBM, variants for viscoelastic fluids have been developed. Keeping in mind our target geometries, we focus here on three dimensional formulations. The first approaches avoided an explicit modeling of a viscoelastic

**TABLE 3** Covered ranges of Wi and $R_\eta$ for existing 3D LB methods.

| Author | max(Wi) | max($R_\eta$) | $R_\eta$ estimation |
|---|---|---|---|
| Malaspinas[25] | 10 | 9 | In 4.3: $R_\nu = 0.1$ and Equation (38) |
| Gupta[26] | 100 | 0.7 | In IV.B: $\frac{\eta_\mathrm{p}}{\eta_\mathrm{A}+\eta_\mathrm{p}} = 0.4$ |
| Ma[29] | 100 | 9 | In 4.1: $\beta = \frac{\mu_\mathrm{s}}{\mu_\mathrm{s}+\mu_\mathrm{p}} = 0.1$ |
| Onishi[30] | ? | 1 | In 3.1: $\beta = \frac{\mu_\mathrm{p}}{\mu_\mathrm{s}+\mu_\mathrm{p}}$ and Table 1: $\beta = 0.5$ |
| Wang[31] | "up to O(1)" | 5 | In II: $\eta_\mathrm{p} = c\eta_\mathrm{s}$ and Figure 9: $c = 5$ |
| Su[33] | 10 | 1 | In II: $\beta = \frac{\eta_\mathrm{s}}{\eta_\mathrm{s}+\eta_\mathrm{p}}$ and In IV.A: $\beta = 0.5$ |
| Gupta[27] | ? | 0.7 | In 2: $\frac{\eta_\mathrm{p}}{\eta_\mathrm{d}} = 0.4$ and $\eta_\mathrm{d} = \eta_\mathrm{A} + \eta_\mathrm{p}$ |
| Kuron[35] | 1 | 9 | In 4.1: $\beta = 0.9$ and Equations (14) and (15) |
| Gupta[36] | 80 | 0.7 | In 3: $\frac{\eta_\mathrm{p}}{\eta_\mathrm{c,d}+\eta_\mathrm{p}} = 0.4$ |
| Onishi[24] | 1000 | 1 | In 3.2: $\frac{\eta_\mathrm{p}}{\eta_\mathrm{s}} = 1$ |

constitutive equation and simply modified the LB collision operator to obtain a basic viscoelastic fluid obeying Jeffery's model.[28] This can also be achieved by the introduction of a second local stress tensor.[32] More advanced approaches include the work of Onishi et al.[24,30] who considered a non-shear-thinning Oldroyd-B model using a microscopic Fokker-Planck equation for the polymer dumbbells. The work of Reference 31 solved the advection part of the model using a second LBM running in parallel to the Navier–Stokes LBM. The same technique was used by Malaspinas et al.[25] and Ma et al.[29] for the Oldroyd-B and FENE-P models. Later, hybrid schemes coupling an LB solver for the solvent to a finite-difference[26,27,36] or finite-volume[35] scheme for the polymer stress (or, alternatively, the polymer conformation) tensor were introduced. To improve numerical stability, some authors propose the inclusion of an artificial diffusivity,[25,29,31,34] which introduces a small error compared to the analytical solution of the constitutive equation. Others perform special decompositions of the stress tensor.[13] Coupling of the resulting polymer stress to the Navier–Stokes LBM can be achieved via the inclusion of point forces or via a modification of the equilibrium populations. Both methods have recently been compared in 2D.[17]

The stable range of Weissenberg numbers covered by existing methods is up to Wi ≈ 10 for the method of Reference 25 and up to Wi ≈ 100 in References 26,29, and 36. However, another stability criterion, which is often overlooked is the viscosity ratio $R_\eta$ as defined in Equation (7). Existing methods often stay at or below $R_\eta = 1$,[26,27,30,31,33] while others report being limited below $R_\eta = 10$[25,29,35] according to Malaspinas et al. due to stability issues. The details are listed in Table 3. Comparing to the rheological data presented in Figures 1 and 2, we conclude that existing LB methods appear to be appropriate only for relatively dilute solutions and in particular do not cover the viscosity ratio required by technologically important cell carrier fluids such alginate and methyl cellulose. We therefore set out to develop a novel viscoelastic LBM scheme which we will present in the next section.

## 4 | NUMERICAL METHODS

Our algorithm contains a Lattice–Boltzmann solver for the Navier–Stokes equations of the solvent, a finite-volume solver for integrating the polymer stress and finally our newly developed viscosity shuffling method.

### 4.1 | Lattice–Boltzmann for Navier–Stokes

The Lattice–Boltzmann method (LBM) has become a standard tool in numerical fluid mechanics,[7] and we therefore only mention the key choices here. Further details can be found in the Appendix E or in literature. We use a D3Q19 lattice in full three dimensions together with a single relaxation time (SRT) collision operator. Various tests with a multiple relaxation time (MRT) collision operator did not show significant differences. Our implementation is based on FluidX3D which has been extensively used and validated in earlier publications.[48,49] The core of the algorithm is implemented in OpenCL and thus capable of running on GPUs from different vendors. Non-periodic boundaries are modeled using the half-way bounce back algorithm. To model fixed inflow/outflow, bounce back boundaries using a Dirichlet boundary condition as described by Krüger et al.[7] are used.

Physical units are mapped to lattice units to obtain a dimensionless relaxation time of 1. The employed lattice dimensions vary for the different applications and are specified below. To drive the flow, we use either a constant body force (modeling a physical pressure gradient) or inflow-outflow boundaries as specified in the different application scenarios below.

## 4.2 | Finite-volume for polymer stress

The spatio-temporal dynamics of the polymer stress $\underline{\tau}$ is given by Equation (1) in the form of an advection-reaction equation. We solve this equation by a finite-volume scheme running in parallel (with identical time step) to the LBM solver. For this, the simulation volume is subdivided in $1 \times 1 \times 1$ (in LU) cubes centered around each lattice node. The average value of $\underline{\tau}$ within these volumes is takes as the value at the lattice node. Advection is handled using the corner transport upwind scheme (CTU).[35] CTU considers the finite volume cell to be virtually displaced by $\vec{u}\Delta t$, where $\vec{u}$ is the local velocity and $\Delta t$ is the size of a time step. The resulting overlap with the neighboring cells (as a fraction of the cell volume) dictates what percentage of the polymer stress currently located at the cell is advected to the respective neighbor. This scheme prevents checkerboard instabilities. The remaining derivatives are calculated using finite differences. At the walls, which coincide with the surfaces of the finite volumes, a zero-flux boundary condition for the stress is used. The source terms are integrated using the Euler method.

To include the polymer stress into the LBM, we use the stress coupling scheme according to Dzanic et al.[17,26,30] Specifically, we implement the LBM collision as follows.

$$f_i\left(\vec{x} + \vec{c}_i\Delta t, t + \Delta t\right) - f_i(\vec{x}, t) = -\frac{\Delta t}{\tau_\mathrm{r}}\left[f_i(\vec{x}, t) - f_i^\mathrm{eq}(\vec{x}, t) + B_i\right]. \tag{8}$$

Here, $f_i$ are the populations, $f_i^\mathrm{eq}$ are the equilibrium populations, $\vec{c}_i$ are the lattice velocities, $\Delta t$ is the time step, $\tau_\mathrm{r}$ is the relaxation time and $B_i$ are the stress contributions defined as follows.

$$B_i = w_i\left(\frac{\vec{c}_i\vec{c}_i}{2c_\mathrm{s}^4} - \frac{\mathbb{1}}{2c_\mathrm{s}^2}\right) : \underline{\tau}'. \tag{9}$$

Here, $w_i$ are the lattice weights, $c_\mathrm{s}$ is the lattice speed of sound and $\underline{\tau}'$ is the stress tensor to be coupled into the LBM. In the case of viscoelastic fluids this typically is the polymer stress tensor. For our method this tensor is modified as described in the following section. The colon denotes the Frobenius inner product. To handle inflow/outflow boundaries, the polymer conformation tensor is specified on the boundary and advected using the corner transport upwind scheme.

## 4.3 | Novel viscosity shuffling

The key difficulty for simulating many realistic viscoelastic fluids is the imbalance between the viscous stress of the solvent and the polymer stress. While the former is handled efficiently and reliably by the LBM streaming-collision scheme, the latter enters the LB equations as an additional source term. The relative magnitude of the two terms is given by the viscosity ratio $R_\eta$ as defined in Equation (7) which for many situations is of the order of $10^2 - 10^3$ (see Figures 1, 2 and Table 2). The key idea of our scheme is to artificially increase the LBM viscous stress while at the same time reducing the polymer stress by the same amount. Starting from Equation (4), we write

$$\underline{\sigma} = 2\eta_\mathrm{s}\underline{D} + \underline{\tau}_\mathrm{shuffle} + \underline{\tau} - \underline{\tau}_\mathrm{shuffle}, \tag{10}$$

with the transferred ("shuffled") stress

$$\underline{\tau}_\mathrm{shuffle} = 2\alpha_\mathrm{s}\eta_\mathrm{p}\underline{D}, \tag{11}$$

containing an arbitrary parameter $\alpha_s$. Finally, this results in

$$\underline{\sigma} = 2\left(\eta_s + \alpha_s\eta_p\right)\underline{D} + \left(\underline{\tau} - 2\alpha_s\eta_p\underline{D}\right). \tag{12}$$

In practice, the shuffling parameter $\alpha_s$ is chosen before the start of the simulation. The LBM solver is run with $\eta_s + \alpha_s\eta_p$ as its viscosity. The polymer stress determined by Equation (1) is reduced by the amount $2\alpha_s\eta_p\underline{D}$ at every time step before $\underline{\tau'} = \underline{\tau} - 2\alpha_s\eta_p\underline{D}$ is coupled into the LBM.

Using this procedure, we balance the stress contributions of the LB and the polymer components which vastly improves numerical stability. We emphasize that, in contrast to other remedies such as adding artificial diffusivity,[25,29,31,34] our viscosity shuffling algorithm is mathematically exact and does not affect the physics of the simulated system. The only trade-off of our viscosity shuffling scheme is that the increased LB viscosity decreases the LB time step if the lattice relaxation time is maintained at its optimal value of 1. In the following section we validate this novel approach against analytical solutions for realistic parameters and compare its accuracy to existing algorithms.

## 5 | VALIDATION AND ACCURACY

To validate our viscosity shuffling algorithm and to assess its accuracy, we compare simulated velocity fields to semi-analytical solutions in planar and cylindrical Poiseuille flow. For the PTT model given in Equation (1) with an additional solvent stress contribution as in Equation (4) a full analytical solution is not known for planar or cylindrical Poiseuille flow. Based on the work of Reference 50 we can nevertheless derive a semi-analytical solution in Appendix B which will serve to validate our numerical algorithm. A validation in simple shear flow can be found in Appendix C.

We start by simulating the alginate and 0.49% methyl cellulose solutions with a viscosity ratio $R_\eta = 48.2 \times 10^3$ and $R_\eta = 18.7$, respectively, in 2D planar Poiseuille flow. In physical units the channel has a height of 20 μm which are discretized with 41 LBM nodes. For the viscosity shuffling, we set $\alpha_s = 1$ here and check different values further below. Along the flow direction, the channel is periodic, and the flow is driven by a pressure gradient of $-1 \times 10^7\ \frac{\text{Pa}}{\text{m}}$ for alginate and approximately $-1.2 \times 10^7\ \frac{\text{Pa}}{\text{m}}$ for methyl cellulose. The velocity field is initialized with zero. For methyl cellulose, we simulate the full temporal evolution with the polymers starting in the unstretched configuration. In the case of alginate, we speed up the convergence and start from a situation in which the polymers are pre-stretched. For this we calculate $\tau_{xx}$ and $\tau_{xy}$ using Equations (B23) and (B10) using the $\dot{\gamma}$ calculated from Equation (B45). The polymer stress is then initialized using these values. After $2 \times 10^9$ LBM time steps for alginate and $5 \times 10^6$ LBM time steps for methyl cellulose corresponding to approximately 1.6 ms and 2.4 s of physical time, respectively, the simulation is stopped and the flow field $u(y)$ is compared to the semi-analytical solution. An artificial increase of the Reynolds number to reduce computational time is possible in principle, but is not employed here to bring out clearly the characteristics of our method. As shown in Figure 3, very good agreement is found. The time evolution of the center-line velocity is shown in Figure D1 of the Appendix. For a quantitative assessment, we compute the L2 error as follows.

$$e_{\text{L2}} = \sqrt{\frac{\sum_i \left[\vec{u}_i - \vec{u}(y_i)\right]^2}{\sum_i \vec{u}(y_i)^2}}. \tag{13}$$

Using the simulated velocities $\vec{u}_i$ and the semi-analytical results $\vec{u}$. This gives $9 \times 10^{-4}$ and $1 \times 10^{-3}$ for alginate and methyl cellulose, respectively. The spatially resolved L1 error defined as follows is shown in Figure D2 in the Appendix.

$$e_{\text{L1}} = \frac{\vec{u}_i - \vec{u}(y_i)}{\vec{u}(y_i)}. \tag{14}$$

These conclusions remain unchanged even when varying the pressure gradient, and thus the flow velocity, over many orders of magnitude as shown in Figure D3A of the Appendix. Similarly, the exact value of $\alpha_s$ does not matter as can be seen in Figure D6.

We proceed to evaluate the viscosity shuffling method for a cylindrical Poiseuille flow. The semi-analytical solution for this situation can be derived similarly as for the planar case and is given in Appendix B. Numerically, the cylindrical situation is slightly more complex due to discretization errors ("staircase effect") when mapping the rounded channel

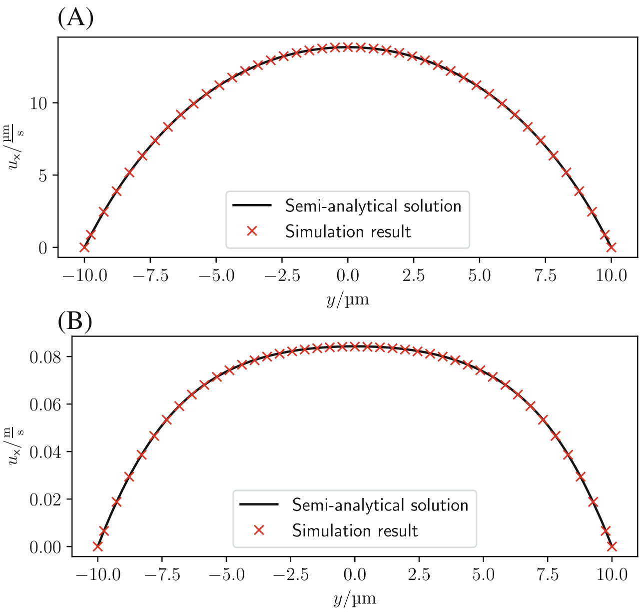

**FIGURE 3** (A) Velocity profile of alginate in planar channel flow. (B) Velocity profile for methyl cellulose. [Colour figure can be viewed at wileyonlinelibrary.com]

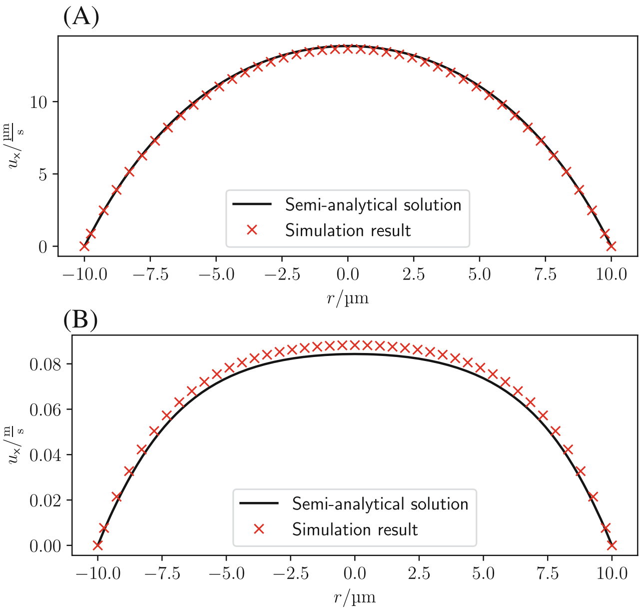

**FIGURE 4** (A) Velocity profile of alginate in cylindrical channel flow. The time evolution of the center-line velocity when starting from a pre-stretched configuration (see main text) is shown in Figure D4. (B) Velocity profile for methyl cellulose. [Colour figure can be viewed at wileyonlinelibrary.com]

walls onto the rectilinear LBM grid.[49] We use the same material parameters as above, but double the pressure gradient to $-2 \times 10^7\ \frac{\mathrm{Pa}}{\mathrm{m}}$ and approximately $-2.5 \times 10^7\ \frac{\mathrm{Pa}}{\mathrm{m}}$, respectively, thereby mirroring the relation in Newtonian Poiseuille flow where twice the pressure is required to obtain the same flow rate in cylindrical compared to planar geometries. The channel has a diameter of $20\,\mu\mathrm{m}$ and is discretized with 41 lattice points in $y$ and $z$ direction. Again, we initialize the polymers in the unstretched state for methyl cellulose and in the stretched state for alginate. The resulting velocity profile can be seen in Figure 4 and shows almost equally good agreement as for the planar case with an L2 error of 0.014 and

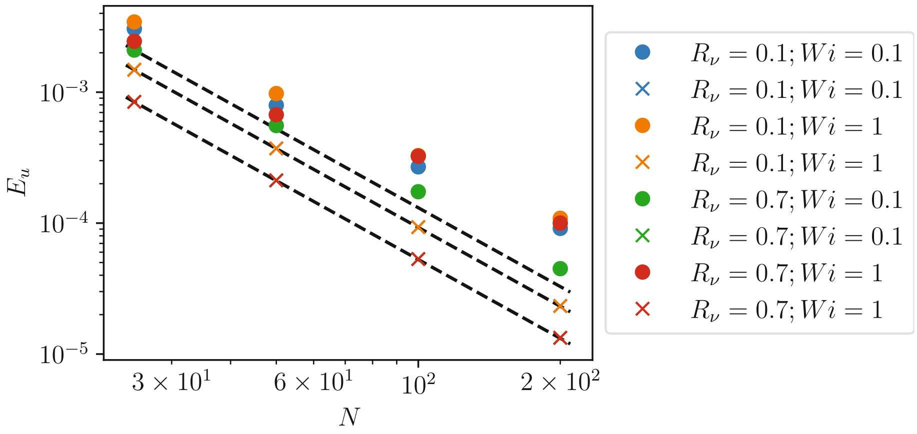

**FIGURE 5** L2 error as defined in Equation (16) from Malaspinas et al.[25] (dots) compared to our algorithm (x) as a function of grid resolution. Blue and green crosses are not visible as they overlap exactly with the orange and red crosses, respectively, showing that the accuracy of our method is independent of Wi in the studied parameter range.

0.06, respectively. The spatially resolved L1 error in Figure D5 of the Appendix shows that this larger average is indeed mainly attributable to the staircase effect as the error near the walls increases significantly. The time evolution of the center-line velocity is shown in Figure D4 of the Appendix. The robustness against pressure gradient changes is shown in Figure D3B of the Appendix.

Finally, we assess the quality of our algorithm by comparing to an existing study on viscoelastic LBM by Malapsinas et al.[25] The authors studied an Oldroyd-B fluid in a planar Poiseuille flow and compared the error in the simulated velocity profile to an exact analytical solution. The Oldroyd-B model is a special case of the PTT model which is obtained by setting $\xi = \epsilon = 0$ in Equation (1) and is thus easily tractable with our code. In Figure 5, we show the L2 error as function of lattice resolution for different values of Wi and $R_\nu$ which is defined as[25]

$$R_\nu = \frac{\nu_s}{\nu_p + \nu_s}, \tag{15}$$

with the kinematic solvent and the polymer viscosity $\nu_s$ and $\nu_p$. We note that this can directly be transformed into the viscosity ratio used above as $\frac{1}{R_\nu} - 1 = R_\eta$. Furthermore, in agreement with Reference 25, also the L2 error is defined differently than above, namely:

$$E_u = \frac{1}{u_{\max}} \sqrt{\frac{1}{N} \sum |u_{\text{simulation}} - u_{\text{theory}}|^2}. \tag{16}$$

At this point, we mention that there is a typographic mistake in eq (61) of Reference 25 where the prefactor should be 8 instead of 4.

As can be seen in Figure 5, the accuracy of our method does not depend on the Weissenberg Number and is generally somewhat better than the method of Reference 25. We note a certain dependence of the accuracy on $R_\nu$ which we consider nevertheless acceptable given the overall smallness of the error. Finally, we find that the error of our method decreases with lattice resolution to the power of −2. The error found by Malaspinas et al. has a similar decrease for small $N$, but sees less reduction at higher $N$.

## 6 | EXAMPLE APPLICATIONS

To illustrate the use of viscosity shuffling in realistic applications, we study three typical experimentally relevant situations. For ease of comparison, we use the 0.49% methyl cellulose in all three situations.

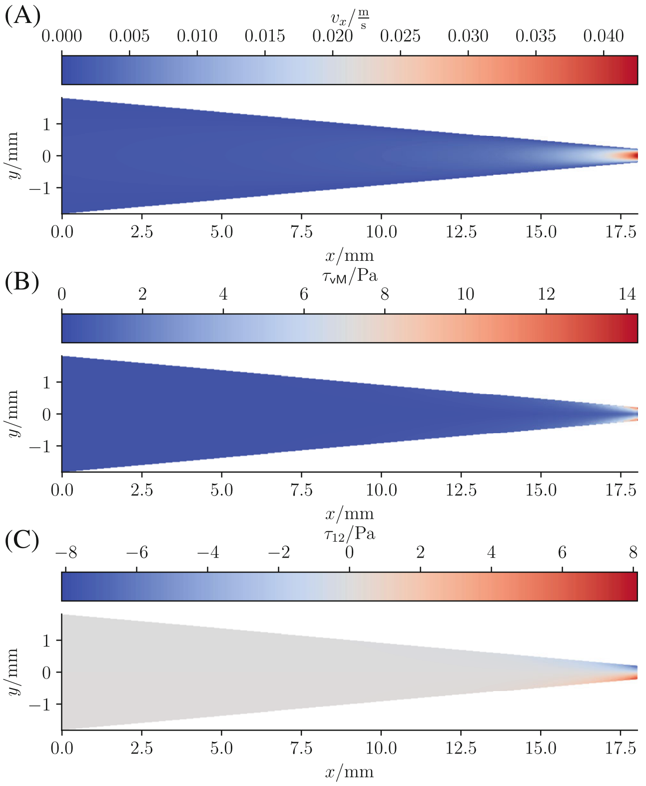

**FIGURE 6** Velocity profile (A), von Mises stress (B) and shear stress (C) for methyl cellulose in a conical nozzle as used for bioprinting. For the calculated viscosity see Figure D7 of the Appendix. [Colour figure can be viewed at wileyonlinelibrary.com]

The first application stems from bioprinting where the bioink is pushed through a conical nozzle.[2–4] The nozzle radius is 1.8 mm at the inlet and 200 μm at the outlet. The nozzle has a length of 18 mm. Due to the difference in inlet/outlet radii, the system cannot be modeled with periodic boundary conditions, and we use inflow/outflow boundary conditions as described in Section 4. The required values for velocity and polymer conformation are obtained from simulations of pipes of the respective radii and a fixed volume flow of $\approx 3\ \frac{\mu\mathrm{L}}{\mathrm{s}}$. The resulting flow field can be seen in Figure 6A. To quantify the total stress as a single number, we use the von Mises stress which is defined as[51]:

$$\tau_{\mathrm{vM}} = \sqrt{\frac{3}{2}\tau_{ij}^{\mathrm{dev}}\tau_{ij}^{\mathrm{dev}}}, \tag{17}$$

with the deviator of the stress tensor defined as follows

$$\tau_{ij}^{\mathrm{dev}} = \tau_{ij} - \frac{1}{3}\tau_{kk}. \tag{18}$$

It can be seen in Figure 6B that the highest stresses arise at the nozzle exit in direct vicinity to the wall. This means that even for fast flows, cells flowing close to the center experience less stress than cells flowing near the walls in agreement with earlier results in Newtonian fluids.[51]

Our next example is the RT-DC geometry in which cells from a reservoir are squeezed through a narrow observation channel[1,52] with a square cross-section of 40 μm × 40 μm. For this simulation we use periodic boundary conditions and a constant body force corresponding to a pressure gradient of $1 \times 10^7\ \frac{\mathrm{Pa}}{\mathrm{m}}$. In Figure 7, we show the velocity profile, the von Mises stress and the shear component of the stress which is the relevant component if a local shear viscosity is to be defined. There are three qualitative differences compared to a purely viscous fluid. Directly after the inlet we find a region of low stress. Due to the fast advection, the polymers, despite being inside the constriction, have not reacted to the increased fluid stress yet. Similarly, directly after the constriction, the high stress inside the observation channel persists

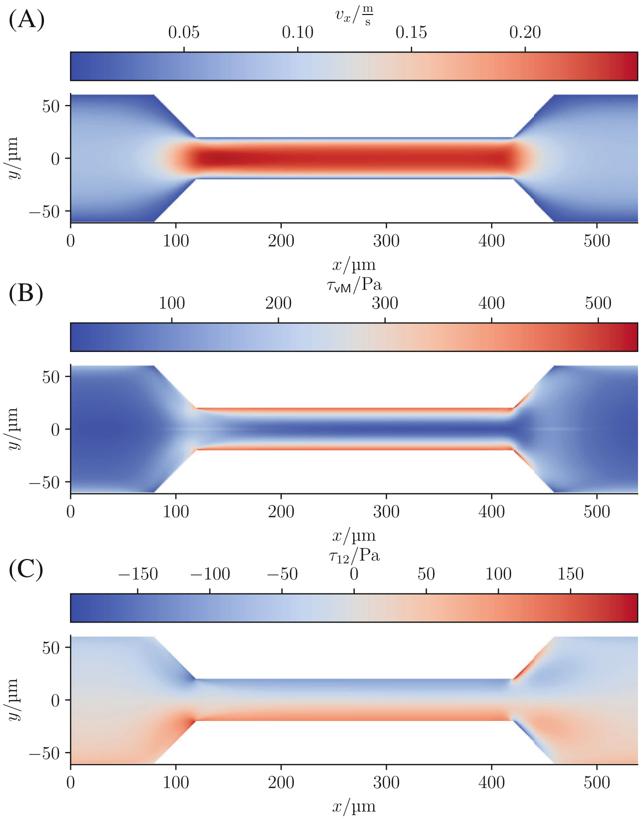

**FIGURE 7** Velocity profile (A), von Mises stress (B) and shear stress (C) for methyl cellulose in a typical RT-DC geometry. For the calculated viscosity see Figure D7. [Colour figure can be viewed at wileyonlinelibrary.com]

over a certain distance that is needed for the polymer stress to decay. If one would divide the stress in these two regions by the strain rate in an attempt to obtain a viscosity one would find a very low and a very high viscosity respectively. These can be outside the range of viscosities, that can be obtained through rheological measurements with the fluid. This effect is even more pronounced along the walls directly after the outlet. Here the viscosities obtained in this manner become negative. Due to the strain rate approaching 0 at several locations within the simulation volume, this calculation often diverges. The clamped result can be seen in Figure D7. These discrepancies, especially the ones at the walls, show the breakdown of the viscosity interpretation in viscoelastic cases and signify the regions of interesting behavior. This also shows why viscoelastic simulations cannot always be replaced by purely viscous models and should be considered despite the high computational cost.

With the third example we demonstrate the versatility of our approach which allows easy coupling to other LBM extensions such as the immersed-boundary method. Here, we include a homogeneously elastic particle as a simple, yet reasonably accurate, model for the mechanics of a living, biological cell.[53] Coupling to the LBM solver is achieved with the immersed-boundary method as described in earlier publications.[54] For simplicity, we consider the viscoelastic fluid inside and outside the cell to be identical. The cell is initially spherical with a radius of 6 μm and possesses a Youngs modulus of 100 Pa and a Poisson ratio of 0.48. It is placed into a shear flow with a shear rate of 400 $\frac{1}{\mathrm{s}}$ where the cell quickly reaches a steady state in which it deforms into a tank-treading ellipsoid. This is in qualitative agreement with simulations[54] and classical theories.[55] For the discretization of the cell we use 5179 tetrahedrons and a radius of 6 lattice units. The lattice with a resolution of 100 lattice points is chosen significantly larger than the cell to assure negligible impact of the walls. The lattice is periodic in $x$ and $z$ direction. At the edges of the simulation box in $y$ direction Dirichlet boundary conditions are imposed.

In the von Mises stress shown in Figure 8 the effect of the cell is clearly visible. We observe four distinct regions of high stress radiating outwards from the cell body. These are particularly pronounced along the longest axis of the deformed cell.

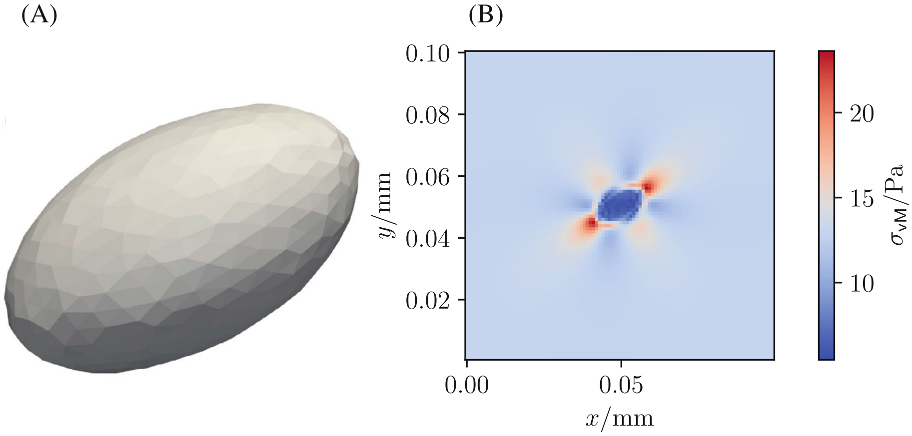

**FIGURE 8** Cell in viscoelastic shear flow. (A) The 3D shape of the deformed cell and (B) a 2D cross-section of the von Mises stress. [Colour figure can be viewed at wileyonlinelibrary.com]

## 7 | SUMMARY AND CONCLUSION

In this work, we developed a novel simulation algorithm for viscoelastic fluids. Our method is based on the LBM for the solvent combined with a finite-volume solver for the polymer dynamics. Its key novel ingredient is the introduction of a shuffling parameter $\alpha_s$ which shifts a substantial part of the polymer stress into the solvent contribution by artificially increasing the solvent viscosity. The algorithm compensates for this extra solvent stress by lowering—by the same amount—the polymer stress thus leaving the total stress invariant. This procedure is mathematically exact and does not introduce any additional physical approximations, but significantly increases numerical stability.

We applied the method to the simulation of two realistic cell carrier fluids: an alginate and a methyl cellulose suspension. For simple situations such as shear and Poiseuille flow, we found very good agreement with (semi-)analytical theories. Importantly, the outcome of the viscosity shuffling simulations is independent of the shuffling parameter $\alpha_s$. We finally demonstrated the usability of our approach in realistic geometries such as constricting microchannels and conical bioprinting nozzles.

## ACKNOWLEDGMENTS

The authors would like to thank the Deutsche Forschungsgemeinschaft (DFG, German Research Foundation) under Project number 326998133, TRR 225 Biofabrication (subprojects B07, B09 and Z01) and the Federal Ministry of Education and Research (BMBF) under Project SOP_Bioprint (Contract Number 13XP5071B) for enabling data collection. Open Access funding enabled and organized by Projekt DEAL.

## DATA AVAILABILITY STATEMENT

The data that support the findings of this study are available from the corresponding author upon reasonable request.

## ORCID

*Richard Kellnberger* https://orcid.org/0009-0003-1782-4735
*Stephan Gekle* https://orcid.org/0000-0001-5597-1160

## REFERENCES

1. Toepfner N, Herold C, Otto O, et al. Detection of human disease conditions by single-cell morphorheological phenotyping of blood. *Elife*. 2018;7:e29213. doi:10.7554/elife.29213
2. Pössl A, Hartzke D, Schmidts TM, Runkel FE, Schlupp P. A targeted rheological bioink development guideline and its systematic correlation with printing behavior. *Biofabrication*. 2021;13(3):035021. doi:10.1088/1758-5090/abde1e
3. Poologasundarampillai G, Haweet A, Jayash SN, Morgan G, Moore JE, Candeo A. Real-time imaging and analysis of cell-hydrogel interplay within an extrusion-bioprinting capillary. *Bioprinting*. 2021;23:e00144. doi:10.1016/j.bprint.2021.e00144
4. O'Connell C, Ren J, Pope L, et al. Correction to: characterizing bioinks for extrusion bioprinting: printability and rheology. In: Crook JM, ed. *3D Bioprinting*. Humana; 2022:C1. doi:10.1007/978-1-0716-0520-2_18

5. Paxton N, Smolan W, Böck T, Melchels F, Groll J, Jungst T. Proposal to assess printability of bioinks for extrusion-based bioprinting and evaluation of rheological properties governing bioprintability. *Biofabrication*. 2017;9(4):044107. doi:10.1088/1758-5090/aa8dd8
6. Alves MA, Oliveira PJ, Pinho FT. Numerical methods for viscoelastic fluid flows. *Annu Rev Fluid Mech*. 2020;53(1):509-541. doi:10.1146/annurev-fluid-010719-060107
7. Krüger T, Kusumaatmaja H, Kuzmin A, Shardt O, Silva G, Viggen EM. *The Lattice Boltzmann Method*. Springer; 2017.
8. Ispolatov I, Grant M. Lattice Boltzmann method for viscoelastic fluids. *Phys Rev E*. 2002;65(5):056704. doi:10.1103/physreve.65.056704
9. Wang D, Tan D, Phan-Thien N. A lattice Boltzmann method for simulating viscoelastic drops. *Phys Fluids*. 2019;31(7):073101. doi:10.1063/1.5100327
10. Jin S, Ouyang J, Wang X, Yang B, Zhou W. Lattice Boltzmann method for the simulation of viscoelastic fluid flows over a large range of Weissenberg numbers. *J Nonnewton Fluid Mech*. 2013;194:42-59. doi:10.1016/j.jnnfm.2012.11.006
11. Giraud L, d'Humires D, Lallemand P. A lattice Boltzmann model for Jeffreys viscoelastic fluid. *Europhys Lett*. 1998;42(6):625-630. doi:10.1209/epl/i1998-00296-0
12. Xie C, Lei W, Wang M. Lattice Boltzmann model for three-phase viscoelastic fluid flow. *Phys Rev E*. 2018;97(2):023312. doi:10.1103/physreve.97.023312
13. Dzanic V, From CS, Sauret E. A hybrid lattice Boltzmann model for simulating viscoelastic instabilities. *Comput Fluids*. 2022;235:105280. doi:10.1016/j.compfluid.2021.105280
14. Frank X, Li HZ. Negative wake behind a sphere rising in viscoelastic fluids: a lattice Boltzmann investigation. *Phys Rev E*. 2006;74(5):056307. doi:10.1103/physreve.74.056307
15. Zou S, Yuan X-F, Yang X, Yi W, Xu X. An integrated lattice Boltzmann and finite volume method for the simulation of viscoelastic fluid flows. *J Nonnewton Fluid Mech*. 2014;211:99-113. doi:10.1016/j.jnnfm.2014.07.003
16. Lee YK, Ahn KH. A novel lattice Boltzmann method for the dynamics of rigid particles suspended in a viscoelastic medium. *J Nonnewton Fluid Mech*. 2017;244:754. doi:10.1016/j.jnnfm.2017.04.007
17. Dzanic V, From CS, Sauret E. Assessment of polymer feedback coupling approaches in simulation of viscoelastic fluids using the lattice Boltzmann method. *Comput Fluids*. 2022;246:105629. doi:10.1016/j.compfluid.2022.105629
18. Sedaghat MH. A hybrid immersed boundary-lattice Boltzmann method for simulation of viscoelastic fluid flows interaction with complex boundaries. *Commun Comput Phys*. 2021;29(5):1411-1445. doi:10.4208/cicp.oa-2019-0158
19. Frantziskonis GN. Lattice Boltzmann method for multimode wave propagation in viscoelastic media and in elastic solids. *Phys Rev E*. 2011;83(6):066703. doi:10.1103/physreve.83.066703
20. Qin S, Jiang M, Ma K, Jin S, Liu Z. Fully resolved simulations of viscoelastic suspensions by an efficient immersed boundary-lattice Boltzmann method. *Particuology*. 2023;75:26-49. doi:10.1016/j.partic.2022.06.004
21. Yoshino M, Toriumi Y, Arai M. Lattice Boltzmann simulation of two-phase viscoelastic fluid flows. *J Comput Sci Tech*. 2008;2(2):330-340. doi:10.1299/jcst.2.330
22. Papenkort S, Voigtmann T. Lattice Boltzmann simulations of a viscoelastic shear-thinning fluid. *J Chem Phys*. 2015;143(4):044512. doi:10.1063/1.4927576
23. Phillips TN, Roberts GW. Lattice Boltzmann models for non-Newtonian flows. *IMA J Appl Math*. 2011;76(5):790-816. doi:10.1093/imamat/hxr003
24. Onishi J, Chen Y, Ohashi H. A lattice Boltzmann model for polymeric liquids. *Int J Comput Fluid D*. 2005;5(1/2):75. doi:10.1504/pcfd.2005.005819
25. Malaspinas O, Fiétier N, Deville M. Lattice Boltzmann method for the simulation of viscoelastic fluid flows. *J Nonnewton Fluid Mech*. 2010;165(23–24):1637-1653. doi:10.1016/j.jnnfm.2010.09.001
26. Gupta A, Sbragaglia M, Scagliarini A. Hybrid lattice Boltzmann/finite difference simulations of viscoelastic multicomponent flows in confined geometries. *J Comput Phys*. 2015;291:177-197. doi:10.1016/j.jcp.2015.03.006
27. Gupta A, Sbragaglia M. Deformation and break-up of viscoelastic droplets using lattice Boltzmann models. *Procedia IUTAM*. 2015;15:215-227. doi:10.1016/j.piutam.2015.04.030
28. Lallemand P, d'Humières D, Luo L-S, Rubinstein R. Theory of the lattice Boltzmann method: three-dimensional model for linear viscoelastic fluids. *Phys Rev E*. 2003;67(2):021203. doi:10.1103/physreve.67.021203
29. Ma J, Wang Z, Young J, Lai JCS, Sui Y, Tian F-B. An immersed boundary-lattice Boltzmann method for fluid-structure interaction problems involving viscoelastic fluids and complex geometries. *J Comput Phys*. 2020;415:109487. doi:10.1016/j.jcp.2020.109487
30. Onishi J, Chen Y, Ohashi H. Dynamic simulation of multi-component viscoelastic fluids using the lattice Boltzmann method. *Phys A Stat Mech Appl*. 2006;362(1):84-92. doi:10.1016/j.physa.2005.09.022
31. Wang D, Tan DS, Khoo BC, Ouyang Z, Phan-Thien N. A lattice Boltzmann modeling of viscoelastic drops' deformation and breakup in simple shear flows. *Phys Fluids*. 2020;32(12):123101. doi:10.1063/5.0031352
32. Dellar PJ. Lattice Boltzmann formulation for linear viscoelastic fluids using an abstract second stress. *SIAM J Sci Comput*. 2014;36(6):A2507-A2532. doi:10.1137/130940372
33. Jin S, Ouyang J, Wang X, Yang B. Lattice Boltzmann method coupled with the Oldroyd-B constitutive model for a viscoelastic fluid. *Phys Rev E*. 2013;88(5):053304. doi:10.1103/physreve.88.053304
34. Wang D, Tan DS, Khoo BC, Ouyang Z, Phan-Thien N. A lattice Boltzmann modeling of the bubble velocity discontinuity (BVD) in shear-thinning viscoelastic fluids. *Phys Fluids*. 2021;33(3):033108. doi:10.1063/5.0042693
35. Kuron M, Stewart C, de Graaf J, Holm C. An extensible lattice Boltzmann method for viscoelastic flows: complex and moving boundaries in Oldroyd-B fluids. *Eur Phys J E*. 2021;44:1. doi:10.1140/epje/s10189-020-00005-6

36. Gupta A, Sbragaglia M. A lattice Boltzmann study of the effects of viscoelasticity on droplet formation in microfluidic cross-junctions. *Eur Phys J E*. 2016;39(1):2. doi:10.1140/epje/i2016-16002-1
37. Büyükurganci B, Basu SK, Neuner M, Guck J, Wierschem A, Reichel F. Shear rheology of methyl cellulose based solutions for cell mechanical measurements at high shear rates. *Soft Matter*. 2023;19(9):1739-1748. doi:10.1039/d2sm01515c
38. Oldroyd JG. Non-Newtonian effects in steady motion of some idealized elasticoviscous liquids. *Proc R Soc Lond A Math Phys Sci*. 1958;245(1241):278-297. doi:10.1098/rspa.1958.0083
39. Bird RB, Dotson PJ, Johnson NL. Polymer solution rheology based on a finitely extensible beadspring chain model. *J Nonnewton Fluid Mech*. 1980;7(2):213-235. doi:10.1016/0377-0257(80)85007-5
40. Bird RB, Curtiss CF, Armstrong RC, Hassager O. *Dynamics of Polymeric Liquids, Volume 2: Kinetic Theory*. Wiley; 1987.
41. Phan-Thien N, Tanner RI. A new constitutive equation derived from network theory. *J Nonnewton Fluid Mech*. 1977;2(4):353-365. doi:10.1016/0377-0257(77)80021-9
42. Phan-Thien N. A nonlinear network viscoelastic model. *J Rheol*. 1978;22(3):259-823. doi:10.1122/1.549481
43. Ferrás LL, Morgado ML, Rebelo M, McKinley GH, Afonso AM. A generalised Phan–Thien–Tanner model. *J Nonnewton Fluid Mech*. 2019;269:88-89. doi:10.1016/j.jnnfm.2019.06.001
44. Carreau PJ. Rheological equations from molecular network theories. *Trans Soc Rheol*. 1972;16(1):99-127.
45. Yasuda K. *Investigation of the Analogies Between Viscometric and Linear Viscoelastic Properties of Polystyrene Fluids*. PhD Thesis. Massachusetts Institute of Technology; 1979. http://hdl.handle.net/1721.1/16043
46. Amorim PA, d'Ávila MA, Anand R, Moldenaers P, Van Puyvelde P, Bloemen V. Insights on shear rheology of inks for extrusion-based 3D bioprinting. *Bioprinting*. 2021;22:e00129. doi:10.1016/j.bprint.2021.e00129
47. Jalaal M, Cottrell G, Balmforth N, Stoeber B. On the rheology of Pluronic F127 aqueous solutions. *J Rheol*. 2017;61(1):139-146. doi:10.1122/1.4971992
48. Lehmann M. *High Performance Free Surface LBM on GPUs*. Thesis. University of Bayreuth; 2021. doi:10.15495/EPub_UBT_00005400
49. Lehmann M, Krause MJ, Amati G, Sega M, Harting J, Gekle S. Accuracy and performance of the lattice Boltzmann method with 64-bit, 32-bit, and customized 16-bit number formats. *Phys Rev E*. 2022;106(1):015308. doi:10.1103/physreve.106.015308
50. Oliveira PJ, Pinho FT. Analytical solution for fully developed channel and pipe flow of Phan-Thien–Tanned fluids. *J Fluid Mech*. 1999;387:271-280. doi:10.1017/S002211209900453X
51. Müller SJ, Fabry B, Gekle S. Predicting cell stress and strain during extrusion bioprinting. *Phys Rev Appl*. 2023;19(6):064061. doi:10.1103/physrevapplied.19.064061
52. Fregin B, Czerwinski F, Biedenweg D, et al. High-throughput single-cell rheology in complex samples by dynamic real-time deformability cytometry. *Nat Commun*. 2019;10(1):1-11. doi:10.1038/s41467-019-08370-3
53. Wohlrab S, Mueller S, Gekle S. Mechanical complexity of living cells can be mapped onto simple homogeneous equivalents. *Biomech Model Mechanobiol*. 2024;23:1067-1076. doi:10.1007/s10237-024-01823-9
54. Müller SJ, Weigl F, Bezold C, et al. A hyperelastic model for simulating cells in flow. *Biomech Model Mechanobiol*. 2021;20(2):509-520. doi:10.1007/s10237-020-01397-2
55. Roscoe R. On the rheology of a suspension of viscoelastic spheres in a viscous liquid. *J Fluid Mech*. 1967;28(2):273-293. doi:10.1017/s002211206700206x
56. Kulicke WM, Kiss G, Porter RS. Inertial normal-force corrections in rotational rheometry. *Rheol Acta*. 1977;16(5):568-572. doi:10.1007/bf01525657
57. Virtanen P, Gommers R, Oliphant TE, et al. SciPy 1.0: fundamental algorithms for scientific computing in python. *Nat Methods*. 2020;17(3):261-272. doi:10.1038/s41592-019-0686-2
58. Guo Z, Zheng C, Shi B. Discrete lattice effects on the forcing term in the lattice Boltzmann method. *Phys Rev E*. 2002;65(4):046308. doi:10.1103/physreve.65.046308

**How to cite this article:** Kellnberger R, Jüngst T, Gekle S. Novel lattice Boltzmann method for simulation of strongly shear thinning viscoelastic fluids. *Int J Numer Meth Fluids*. 2025;97(2):164-187. doi: 10.1002/fld.5335

## APPENDIX A. RHEOLOGY MEASUREMENTS OF ALGINATE SOLUTIONS

The solutions were prepared by dissolving alginate (DuPont VIVAPHARM Alginate PH176) in ultrapure water at a ratio of 40 $\frac{\text{mg}}{\text{mL}}$, which here is refereed to as 4% w/v. To ensure homogeneous dissolution, the material was stored at 37°C for 24 h and regularly mixed to ensure complete dissolution. The measurements were conducted with a 25 mm plate-plate geometry at a 500 μm gap on a rheometer (Anton paar MCR 702). A solvent trap was used to limit evaporation. All measurements were done at a set temperature of 25°C as shear rate sweep. Data is agglomerated from 21 independent measurements. The first normal stress difference $N_1$ is calculated from the measured normal force using the following equation[56]:

$$N_1 = \frac{2F}{\pi R^2} + \frac{3}{20}\rho\omega^2 R^2, \tag{A1}$$

where $F$ is the measured normal force, $R$ is the radius of the rheometer, $\rho$ is the density of the fluid and $\omega$ is the angular velocity of the rheometer. The second term is usually omitted and as we found it to matter little, and as the quality of the data we have available is too limited to warrant such detailed corrections, we also choose to omit it. A cone-rheometer would be preferred here, but as $N_2 = 0$ for PTT with $\xi = 0$, the difference is negligible.

## APPENDIX B. SEMI-ANALYTICAL SOLUTION FOR POISEUILLE FLOWS OF PTT FLUIDS WITH SOLVENT VISCOSITY

Our derivation is similar to the one in Oliveira.[50] The origin is placed in the center of the channel. The $x$-axis points in flow direction. We solve both the three dimensional and the two dimensional case. In three dimensions we pick cylindrical coordinates as follows.

$$x = x, \tag{B1}$$

$$y = r\cos\varphi, \tag{B2}$$

$$z = r\sin\varphi. \tag{B3}$$

This unusual choice is to keep the coordinate systems consistent between the two- and three dimensional cases. For two dimensions the $y$-axis points along the velocity gradient. This follows from the 3D case limiting $\varphi$ to $\varphi \in \{0, \pi\}$. Consequently, we define $r = |y|$ in the 2D case. Note, that in 2D this leads to the sign being tracked explicitly as follows.

$$\frac{\partial}{\partial r} = \mathrm{sgn}(y)\frac{\partial}{\partial y}. \tag{B4}$$

For both Poiseuille flow and shear flow, symmetry dictates, that the velocity is unidirectional:

$$\vec{u} = u_x(r)\hat{e}_x. \tag{B5}$$

We also define the shear rate as follows.

$$\dot{\gamma}(r) = \frac{\partial u_x}{\partial r} \leq 0. \tag{B6}$$

Note, that with this the shear rate is always negative. Also, $\dot{\gamma}$ is a constant for pure shear flow.

We start with the solutions of the constitutive equation.

### B.1 Shear solutions

In two dimensions, the constitutive Equation (1) for $\xi = 0$ in steady state easily reduces to the following. Note, that $\underline{\tau}$ is symmetric.

$$\exp\left(\frac{\epsilon\lambda}{\eta_\mathrm{p}}\mathrm{Tr}\underline{\tau}\right)\tau_{xx} = 2\lambda\,\mathrm{sgn}(y)\dot{\gamma}\tau_{xy}, \tag{B7}$$

$$\exp\left(\frac{\epsilon\lambda}{\eta_\mathrm{p}}\mathrm{Tr}\underline{\tau}\right)\tau_{xy} = \eta_\mathrm{p}\,\mathrm{sgn}(y)\dot{\gamma}. \tag{B8}$$

With $\mathrm{Tr}\underline{\tau} = \tau_{xx}$. Note that all other components aside from $\tau_{xx}$ and $\tau_{xy}/\tau_{yx}$ are zero. We define $\tau_{xr} = \tau_{xy}\mathrm{sgn}(y) \leq 0$ to get the following.

$$\exp\left(\frac{\epsilon\lambda}{\eta_\mathrm{p}}\mathrm{Tr}\underline{\tau}\right)\tau_{xx} = 2\lambda\dot{\gamma}\tau_{xr}, \tag{B9}$$

$$\exp\left(\frac{\epsilon\lambda}{\eta_{\mathrm{p}}}\mathrm{Tr}\underline{\tau}\right)\tau_{xr} = \eta_{\mathrm{p}}\dot{\gamma}. \tag{B10}$$

The three dimensional case yields the same formula using significantly more math. We set $\xi = 0$ and start from the velocity gradient.

$$\nabla\vec{u} = \frac{\partial u_x}{\partial r}\hat{e}_r \otimes \hat{e}_x. \tag{B11}$$

This, together with the general formula for $\underline{\tau}$,

$$\underline{\tau} = \tau_{ij}\hat{e}_i \otimes \hat{e}_j, \tag{B12}$$

is used to find the non-zero terms of the upper convected derivative in steady state as follows.

$$\begin{aligned}(\nabla\vec{u})^{\mathrm{T}} \cdot \underline{\tau} = \frac{\partial u_x}{\partial r}\hat{e}_x \otimes \hat{e}_r\big(&\tau_{xx}\hat{e}_x \otimes \hat{e}_x + \tau_{xr}\hat{e}_x \otimes \hat{e}_r + \tau_{x\varphi}\hat{e}_x \otimes \hat{e}_\varphi \\ &+ \tau_{rx}\hat{e}_r \otimes \hat{e}_x + \tau_{rr}\hat{e}_r \otimes \hat{e}_r + \tau_{r\varphi}\hat{e}_r \otimes \hat{e}_\varphi \\ &+ \tau_{\varphi x}\hat{e}_\varphi \otimes \hat{e}_x + \tau_{\varphi r}\hat{e}_\varphi \otimes \hat{e}_r + \tau_{\varphi\varphi}\hat{e}_\varphi \otimes \hat{e}_\varphi\big).\end{aligned} \tag{B13}$$

With the orthonormality

$$\hat{e}_a \otimes \hat{e}_b\hat{e}_c \otimes \hat{e}_d = \hat{e}_a\hat{e}_b^{\mathrm{T}}\hat{e}_c\hat{e}_d^{\mathrm{T}} = \hat{e}_a(\hat{e}_b \cdot \hat{e}_c)\hat{e}_d^{\mathrm{T}} = \hat{e}_a(\delta_{bc})\hat{e}_d^{\mathrm{T}} = \delta_{bc}\hat{e}_a \otimes \hat{e}_d, \tag{B14}$$

we can reduce this to the following.

$$(\nabla\vec{u})^{\mathrm{T}} \cdot \underline{\tau} = \frac{\partial u_x}{\partial r}\big(\tau_{rx}\hat{e}_x \otimes \hat{e}_x + \tau_{rr}\hat{e}_x \otimes \hat{e}_r + \tau_{r\varphi}\hat{e}_x \otimes \hat{e}_\varphi\big). \tag{B15}$$

The second non-zero term in the upper convected derivative due to the symmetry of $\underline{\tau}$ is the transpose of this. Together with the strain rate tensor, which is calculated using the velocity gradient from above, the complete constitutive equation reads:

$$\begin{aligned}0 = &\frac{\partial u_x}{\partial r}\big[2\tau_{rx}\hat{e}_x \otimes \hat{e}_x + \tau_{rr}(\hat{e}_x \otimes \hat{e}_r + \hat{e}_r \otimes \hat{e}_x) + \tau_{r\varphi}\big(\hat{e}_x \otimes \hat{e}_\varphi + \hat{e}_\varphi \otimes \hat{e}_x\big)\big] \\ &- \exp\left(\frac{\epsilon\lambda}{\eta_{\mathrm{p}}}\mathrm{Tr}\underline{\tau}\right)\frac{\underline{\tau}}{\lambda} + \frac{\eta_{\mathrm{p}}}{\lambda}\frac{\partial u_x}{\partial r}(\hat{e}_r \otimes \hat{e}_x + \hat{e}_x \otimes \hat{e}_r).\end{aligned} \tag{B16}$$

We separate this equation by components, meaning if $\hat{e}_i \otimes \hat{e}_j$ does not appear in this equation $\tau_{ij} = 0$.

$$0 = \frac{\partial u_x}{\partial r}[2\tau_{rx}\hat{e}_x \otimes \hat{e}_x] - \exp\left(\frac{\epsilon\lambda}{\eta_{\mathrm{p}}}\mathrm{Tr}\underline{\tau}\right)\frac{\underline{\tau}}{\lambda} + \frac{\eta_{\mathrm{p}}}{\lambda}\frac{\partial u_x}{\partial r}(\hat{e}_r \otimes \hat{e}_x + \hat{e}_x \otimes \hat{e}_r). \tag{B17}$$

The symmetry of $\underline{\tau}$ also holds in cylindrical coordinates, meaning $\tau_{rx} = \tau_{xr}$. We reorder accordingly.

$$\exp\left(\frac{\epsilon\lambda}{\eta_{\mathrm{p}}}\mathrm{Tr}\underline{\tau}\right)\frac{\underline{\tau}}{\lambda} = \dot{\gamma}[2\tau_{xr}\hat{e}_x \otimes \hat{e}_x] + \frac{\eta_{\mathrm{p}}}{\lambda}\dot{\gamma}(\hat{e}_r \otimes \hat{e}_x + \hat{e}_x \otimes \hat{e}_r). \tag{B18}$$

We separate the components once more. Yielding two unique equations.

$$\exp\left(\frac{\epsilon\lambda}{\eta_{\mathrm{p}}}\mathrm{Tr}\underline{\tau}\right)\tau_{xx} = 2\lambda\dot{\gamma}\tau_{xr}, \tag{B19}$$

$$\exp\left(\frac{\epsilon\lambda}{\eta_{\mathrm{p}}}\mathrm{Tr}\underline{\tau}\right)\tau_{xr} = \eta_{\mathrm{p}}\dot{\gamma}. \tag{B20}$$

The trace con be found to be:

$$\mathrm{Tr}\underline{\tau} = \tau_{xx} + \tau_{rr} + \tau_{\varphi\varphi} = \tau_{xx}. \tag{B21}$$

As stated above this solution has the same form as for the two dimensional case. Therefore, the following holds for both cases. We eliminate $\tau_{xr}$ yielding the following.

$$\exp\left(2\frac{\epsilon\lambda}{\eta_\mathrm{p}}\mathrm{Tr}\underline{\tau}\right)\tau_{xx} = 2\lambda\dot{\gamma}^2\eta_\mathrm{p}. \tag{B22}$$

This is solved by the Lambert $W$ function as follows.

$$\tau_{xx} = \frac{\eta_\mathrm{p}}{2\epsilon\lambda}W_0\left(4\epsilon\lambda^2\dot{\gamma}^2\right). \tag{B23}$$

As already mentioned above most components of $\underline{\tau}$ are zero, using specifically

$$0 = \begin{cases} \tau_{yy} = \sigma_{yy}, & \text{in 2D} \\ \tau_{rr} = \sigma_{rr}, & \text{in 3D} \end{cases}, \tag{B24}$$

yields the first normal stress difference $N_1$ as follows.

$$N_1 = \sigma_{xx} - \begin{cases} \sigma_{yy}, & \text{in 2D} \\ \sigma_{rr}, & \text{in 3D} \end{cases} = \tau_{xx} = \frac{\eta_\mathrm{p}}{2\epsilon\lambda}W_0\left(4\epsilon\mathrm{Wi}^2\right). \tag{B25}$$

The second normal stress difference, which is defined as follows, is zero on account of the components in the equation being zero.

$$N_2 = \begin{cases} \sigma_{yy} - \sigma_{zz} = \tau_{yy} - \tau_{zz}, & \text{in 2D} \\ \sigma_{rr} - \sigma_{\varphi\varphi} = \tau_{rr} - \tau_{\varphi\varphi}, & \text{in 3D} \end{cases} = 0. \tag{B26}$$

For the viscosity, we insert this into Equation (B10) and retrieve the following.

$$\eta = \frac{\sigma_{xr}}{\dot{\gamma}}, \tag{B27}$$

$$= \frac{\tau_{xr} + \eta_\mathrm{s}\dot{\gamma}}{\dot{\gamma}}, \tag{B28}$$

$$= \eta(\dot{\gamma}) = \frac{\eta_\mathrm{p}}{\exp\left[0.5W_0\left(4\epsilon\mathrm{Wi}^2\right)\right]} + \eta_\mathrm{s}. \tag{B29}$$

With $\sigma_{xr} = \sigma_{xy}\mathrm{sgn}(y) \leq 0$ in the 2D case analogous to $\tau_{xr}$. This concludes the relevant solutions for shear flow. However, these equations also hold for Poiseuille flow. Next we calculate the velocity profile for Poiseuille flow.

### B.2 Velocity profile

We start with the Navier–Stokes equation (neglecting gravity), which reads as follows.

$$\rho\frac{\mathrm{D}\vec{u}}{\mathrm{D}t} = -\nabla p + \nabla\cdot\underline{\sigma}. \tag{B30}$$

In steady state for this geometry in two dimensions, this reduces to the following.

$$\frac{\partial\sigma_{xr}}{\partial r} = \frac{\partial p}{\partial x}. \tag{B31}$$

In three dimensions there is a slight difference. We start from the stress.

$$\underline{\sigma} = \underline{\tau} + 2\eta_{\mathrm{s}}\underline{D} = \underline{\tau} + \eta_{\mathrm{s}}(\hat{e}_x \otimes \hat{e}_r + \hat{e}_r \otimes \hat{e}_x). \tag{B32}$$

Therefor as seen for $\underline{\tau}$ above, $\underline{\sigma}$ also only has $\sigma_{xx}$, $\sigma_{xr}$, $\sigma_{rx}$ components. Furthermore, from symmetry $x$ and $\varphi$ derivatives of $\underline{\sigma}$ are zero. This reduces the divergence to the following.

$$\nabla \cdot \sigma = \frac{\partial \sigma_{xr}}{\partial r}\hat{e}_x + \frac{\sigma_{xr}}{r}\hat{e}_x. \tag{B33}$$

Notably this leads to a different reduced Cauchy momentum equation than for the 2D case.

$$\frac{\partial \sigma_{xr}}{\partial r} + \frac{\sigma_{xr}}{r} = \frac{\partial p}{\partial x}. \tag{B34}$$

However, due to the convenient form of the additional term both cases are solved by the following.

$$\sigma_{xr} = \frac{\partial p}{\partial x}\frac{r}{2^j}. \tag{B35}$$

Here $j$ is 0 for the two dimensional case and 1 in the three dimensional flow. From here the solution is independent of the dimensionality again. The total stress experienced by the fluid is the one described by the constitutive equation plus the solvent contribution, which can also be written as follows.

$$\tau_{xr} = \partial_x p \frac{r}{2^j} - \eta_{\mathrm{s}}\dot{\gamma}. \tag{B36}$$

Dividing Equation (B9) by Equation (B10) leads to the following relation.

$$\tau_{xx} = \frac{2\lambda}{\eta_{\mathrm{p}}}\tau_{xr}^2 = \frac{2\lambda}{\eta_{\mathrm{p}}}\left(\partial_x p \frac{r}{2^j} - \eta_{\mathrm{s}}\dot{\gamma}\right)^2. \tag{B37}$$

Inserting this back into Equation (B10) yields the following.

$$\dot{\gamma} = \exp\left(\frac{2\epsilon\lambda^2}{\eta_{\mathrm{p}}^2}\left[\partial_x p \frac{r}{2^j} - \eta_{\mathrm{s}}\dot{\gamma}\right]^2\right)\frac{1}{\eta_{\mathrm{p}}}\left(\partial_x p \frac{r}{2^j} - \eta_{\mathrm{s}}\dot{\gamma}\right). \tag{B38}$$

This cannot be integrated as easily as without $\eta_{\mathrm{s}}$, and is only solvable semi-analytically.

$$1 = \exp\left(\frac{2\epsilon\lambda^2}{\eta_{\mathrm{p}}^2}\left[\partial_x p \frac{r}{2^j} - \eta_{\mathrm{s}}\dot{\gamma}\right]^2\right)\frac{1}{\eta_{\mathrm{p}}}\left(\partial_x p \frac{r}{2^j\dot{\gamma}} - \eta_{\mathrm{s}}\right), \tag{B39}$$

$$0 = \frac{2\epsilon\lambda^2}{\eta_{\mathrm{p}}^2}\left[\partial_x p \frac{r}{2^j} - \eta_{\mathrm{s}}\dot{\gamma}\right]^2 - \ln \eta_{\mathrm{p}} + \ln\left(\partial_x p \frac{r}{2^j\dot{\gamma}} - \eta_{\mathrm{s}}\right), \tag{B40}$$

$$0 = 2\epsilon\lambda^2\dot{\gamma}^2\left[\partial_x p \frac{r}{2^j\dot{\gamma}\eta_{\mathrm{p}}} - \frac{\eta_{\mathrm{s}}}{\eta_{\mathrm{p}}}\right]^2 + \ln\left(\partial_x p \frac{r}{2^j\dot{\gamma}\eta_{\mathrm{p}}} - \frac{\eta_{\mathrm{s}}}{\eta_{\mathrm{p}}}\right). \tag{B41}$$

This has the following form

$$0 = ab^2 + \ln b. \tag{B42}$$

This can be solved using the Lambert $W$ function as follows.

$$b = \sqrt{\frac{W_0(2a)}{2a}}. \tag{B43}$$

Resolving for $r$ yields the following.

$$r = \frac{2^j \eta_s}{\partial_x p} \dot{\gamma} - \frac{\eta_p 2^{j-1}}{\lambda \sqrt{\epsilon} \partial_x p} \sqrt{W_0\left(4\epsilon\lambda^2\dot{\gamma}^2\right)}. \tag{B44}$$

We notice, that this is the solution for a Poiseuille flow with viscosity $\eta_s$ expanded by a term that applies a nonuniform scaling of the profile along the $r$-axis towards higher radii. We simplify again using $c < 0$ and $d > 0$.

$$r = c\dot{\gamma} - R_\eta \frac{c}{d} \sqrt{W_0\left(d^2\dot{\gamma}^2\right)}. \tag{B45}$$

Finally this function needs to be inverted. This needs to be done numerically. We calculate a range of $\dot{\gamma}$ from 0 to $\frac{R}{c}$ with a small step interval. Here $R$ is the radius of the channel or pipe. This is guaranteed to contain all relevant radii. We flip the axis and integrate numerically using `scipy.integrate.cumulative_trapezoid`.[57] This is very accurate as we conveniently picked the spacing of our now $x$-axis in a way, that the $y$-axis ($\dot{\gamma}$) varies little for each step. From the recovered curve $u$ is calculated at each required $r$ through linear interpolation.

## APPENDIX C. VALIDATION IN PURE SHEAR FLOW

As additional quantitative validation, we simulate a pure shear flow driven by imposing a fixed velocity at the top and bottom of the computational box and using periodic boundary conditions in the other two directions. The box dimension is $2 \times 43 \times 2$. We use PTT with the methyl cellulose parameters and vary the shear rate to cover the full range starting from the zero-shear all the way to the infinite-shear plateau displayed in Figure 2 of the main text. The shuffling is fixed at $\alpha_s = 1$ and the viscosity as function of shear rate is computed by dividing the total fluid stress at the center of the box by the shear rate. Figure C1A shows that our simulations are in very good agreement with the semi-analytical solution with a maximum error of $2 \times 10^{-11}$. Importantly, we show in Figure C1B that this very good agreement is independent of the shuffling parameter $\alpha_s$.

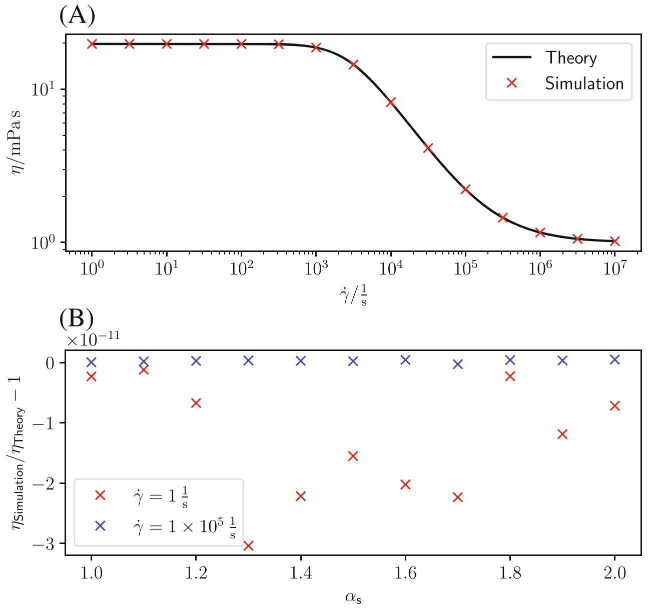

**FIGURE C1** (A) The local viscosity determined by a shear flow simulation is in very good agreement with the semi-analytical theory. (B) The error is negligibly small and independent of the shuffling parameter $\alpha_s$.

## APPENDIX D. SUPPLEMENTARY FIGURES

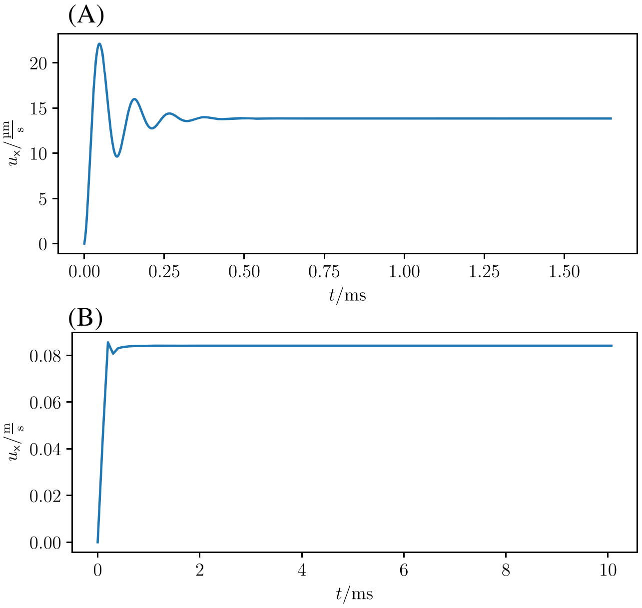

**FIGURE D1** Time evolution of the center-line velocity of an alginate (A) and methyl cellulose (B) solution in planar Poiseuille flow as seen in Figure 3. [Colour figure can be viewed at wileyonlinelibrary.com]

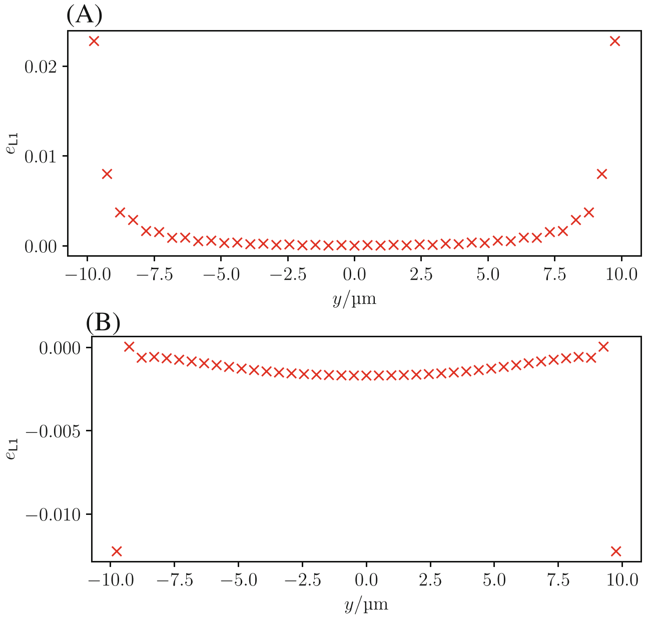

**FIGURE D2** L1 error of the velocity profile in Figure 3 with respect to the semi-analytical theory in a planar Poiseuille flow for alginate (A) and methyl cellulose (B). The relative error is highest near the wall as the velocity is lowest there, but also because the simple half way bounce back boundaries used here allow some slip along the wall. [Colour figure can be viewed at wileyonlinelibrary.com]

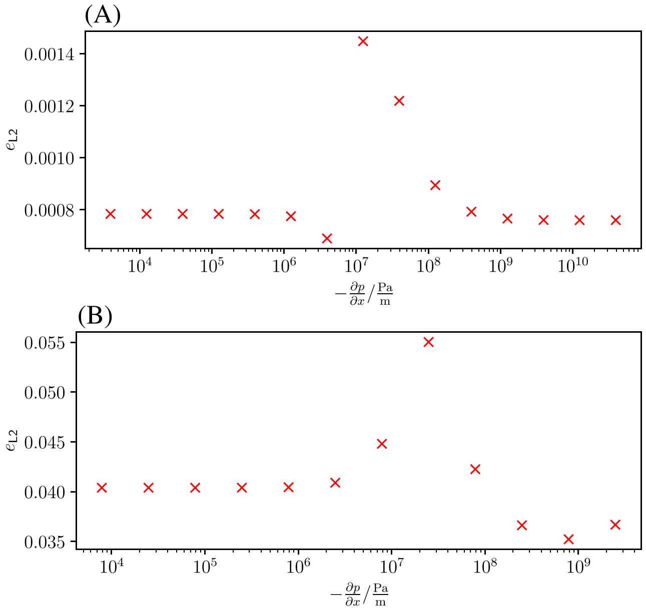

**FIGURE D3** L2 error of the velocity for a planar (A) and a cylindrical (B) Poiseuille flow of methyl cellulose at different pressure gradients. The peak in the error profile appears when the average shear rate across the channel corresponds to the maximum slope in the viscosity profile of Figure C1. [Colour figure can be viewed at wileyonlinelibrary.com]

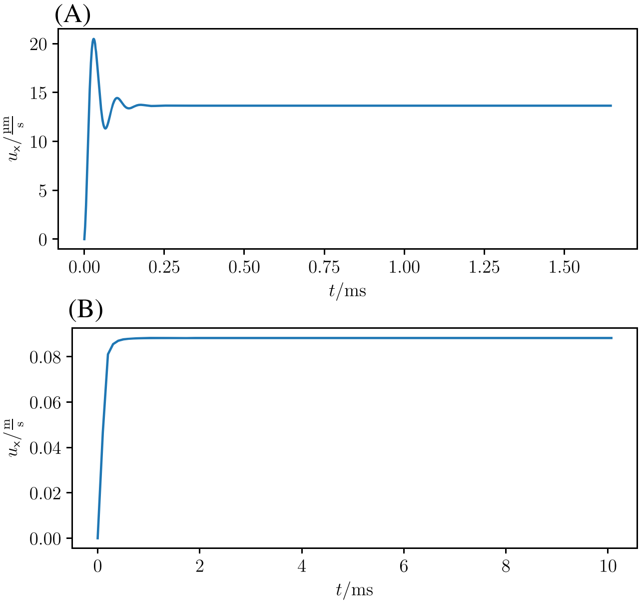

**FIGURE D4** Time evolution of the center-line velocity of an alginate (A) and methyl cellulose (B) cylindrical Poiseuille flow as seen in Figure 4. [Colour figure can be viewed at wileyonlinelibrary.com]

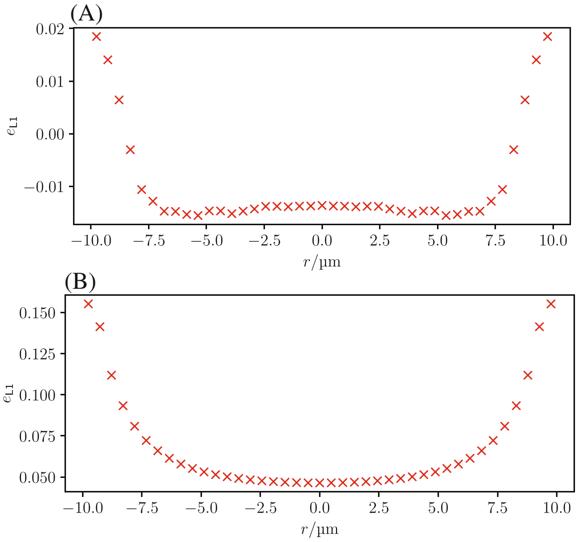

**FIGURE D5** L1 error of the velocity profile in 4 with respect to the semi-analytical theory in a cylindrical Poiseuille flow for alginate (A) and methyl cellulose (B). The relative error is highest near the wall as the velocity is lowest there, but also because the simple half way bounce back boundaries used here allow some slip along the wall.

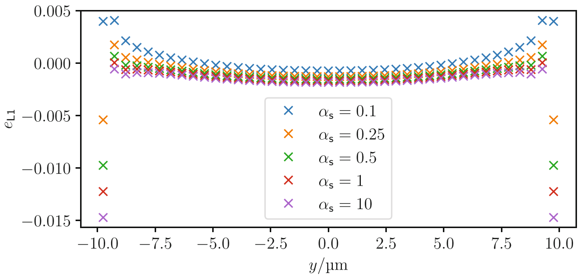

**FIGURE D6** In planar Poiseuille flow, the result is near identical for different $\alpha_s$. The error reveals minor differences. Aside from the wall nodes, the largest error appears for small shuffle fractions. For large ones, the error appears to become independent of $\alpha_s$. This indicates, that the observed difference might be due to the Mach number changing for different $\alpha_s$ and not due to the shuffling itself. This is due lower $\alpha_s$ leading to lower LBM viscosities and such to higher Mach numbers.

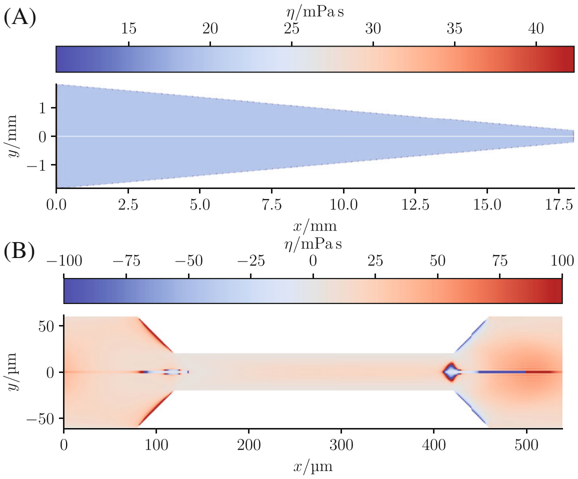

**FIGURE D7** "Viscosity" in a Nozzle (A) and RT-DC channel (B) calculated by dividing $\tau_{12}$ by the respective strain rate and adding the solvent viscosity. This diverges along the center line, and thus it has been excluded. For the RT-DC channel this results in very large and unphysical values, which had to be clamped. The flow and stresses in these geometries can be seen in Figures 6 and 7.

## APPENDIX E. LATTICE–BOLTZMANN IMPLEMENTATION

An excellent overview on LBMs can be found in the book by Krüger et al. on the subject.[7] Our implementation mostly follows the book, though some implementation details differ. We mention the most important basics of LBM here and recommend the book for further reading. Instead of solving the Navier–Stokes equation LBM solves the Boltzmann equation for fluid particle distributions. The Boltzmann equation is discretized both in space $\vec{x}$ and time $t$. Also, the velocity is limited to discrete values $\vec{c}_i$, the so-called velocity sets. The velocity sets are usually denoted as D$d$Q$q$, with $d$ being the number of dimensions and $q$ being the number of discrete velocities. We use D3Q19. Its 19 velocities can be found in Equation (E9). The density is split into the so-called populations $f_i(\vec{x}, t)$, which are parts of the density moving along a certain discrete velocity at a certain discrete point in time at a certain discrete point in space. With these discretizations the Boltzmann equation reads as follows.

$$f_i\left(\vec{x}+\vec{c}_i\Delta t, t+\Delta t\right) = f_i(\vec{x}, t) + \Omega_i(\vec{x}, t). \tag{E1}$$

Here $\Delta t$ is the duration of a time step (distance between the discrete points in time) and $\Omega_i(\vec{x}, t)$ is the collision operator. The equation describes the populations moving along the discrete velocities to a neighboring point (streaming) while exchanging momentum modeled by the collision operator (collision). The collision operator redistributes the populations, that meet at any given lattice point. This is highly complex and is therefore usually approximated using the Bhatnagar–Gross–Krook (BGK) operator, which reads as follows.

$$\Omega_i = -\frac{f_i - f_i^{\mathrm{eq}}}{\tau_{\mathrm{r}}}\Delta t. \tag{E2}$$

Here $\tau_{\mathrm{r}}$ is the relaxation time and $f_i^{\mathrm{eq}}$ are the equilibrium populations defined as follows.

$$f_i^{\mathrm{eq}} = w_i \rho \left[1 + \frac{\vec{u}\cdot\vec{c}_i}{c_{\mathrm{s}}^2} + \frac{\left(\vec{u}\cdot\vec{c}_i\right)^2}{2c_{\mathrm{s}}^4} + \frac{\vec{u}\cdot\vec{u}}{2c_{\mathrm{s}}^2}\right]. \tag{E3}$$

Here $\vec{u}$ is the local fluid velocity, $\rho$ is the local density, $w_i$ are the lattice weights associated to the chosen velocity set (given in Equation (E10) for D3Q19) and $c_{\mathrm{s}}$ is the lattice speed of sound defined as follows.

$$c_{\mathrm{s}}^2 = \frac{1}{3}\frac{\Delta x^2}{\Delta t^2}. \tag{E4}$$

Here $\Delta x$ is the distance between two discrete lattice points. The LBM equation with BGK therefore takes the shape of a relaxation towards equilibrium:

$$f_i\left(\vec{x}+\vec{c}_i\Delta t, t+\Delta t\right) - f_i(\vec{x}, t) = -\frac{\Delta t}{\tau_{\mathrm{r}}}\left[f_i(\vec{x}, t) - f_i^{\mathrm{eq}}(\vec{x}, t)\right]. \tag{E5}$$

It should be noted, that this is the simple case for a Newtonian fluid. If additional (external) forces are to be considered, additional terms are added on the right-hand side to account for these. For the forces used to drive the simple periodic flows and the forces from the IBM used to simulate cells, we use the algorithm presented by Guo et al.[58] The following equations relate the discrete quantities back to the physical quantities.

$$\rho = \sum_i f_i^{\mathrm{eq}} = \sum_i f_i, \tag{E6}$$

$$\rho\vec{u} = \sum_i \vec{c}_i f_i^{\mathrm{eq}} = \sum_i \vec{c}_i f_i, \tag{E7}$$

$$\frac{\eta}{\rho} = c_{\mathrm{s}}^2\left(\tau_{\mathrm{r}} - \frac{\Delta t}{2}\right). \tag{E8}$$

Here $\eta$ is the viscosity. These equations are typically solved in lattice units (LU). These result from fixing three values in LU and calculating conversion factors for all other units accordingly from these. The physical values are then divided by these scaling factors. This is mathematically identical to scaling the whole equation and can be used to simplify the calculations and to keep the values in a range optimal for computation. We pick $\rho_{\mathrm{LU}} = 1$ and $\eta_{\mathrm{LU}} = \frac{1}{6}$ as is typically done. Naturally $\Delta x_{\mathrm{LU}} = 1$ and $\Delta t_{\mathrm{LU}} = 1$. A convenient third scale is the resolution, meaning the relation of $\Delta x$ to the size of the system, which we pick depending on the geometry. The relaxation time can be freely chosen, but is ideal at unity in LU. The LBM scheme with the BGK operator is called single relaxation time (SRT). There are generalizations for two relaxation times (TRT) and for one relaxation time per $i$ (multi relaxation time, MRT). We found the more complex schemes to rarely yield worthwhile improvement and stick to SRT. While there are multiple valid options we use D3Q19 as the velocity set. The 19 velocities and their weights are noted in the following.

$$\frac{\Delta t}{\Delta x}\vec{c}_i = \left\{\begin{matrix} 0 & 1 & -1 & 0 & 0 & 0 & 0 & 1 & -1 & 1 & -1 & 0 & 0 & 1 & -1 & 1 & -1 & 0 & 0 \\ 0 & 0 & 0 & 1 & -1 & 0 & 0 & 1 & -1 & 0 & 0 & 1 & -1 & -1 & 1 & 0 & 0 & 1 & -1 \\ 0 & 0 & 0 & 0 & 0 & 1 & -1 & 0 & 0 & 1 & -1 & 1 & -1 & 0 & 0 & -1 & 1 & -1 & 1 \end{matrix}\right\}, \tag{E9}$$

where each column is a vector.

$$w_i = \begin{cases} \frac{1}{3}, & i = 0 \\ \frac{1}{18}, & 1 \leq i \leq 6 \\ \frac{1}{36}, & \text{otherwise} \end{cases} . \tag{E10}$$